

A systematic comparison of ionization temperatures between ionizing and recombining plasmas in supernova remnants

Shigeo YAMAUCHI,^{1,*} Masayoshi NOBUKAWA,² and Katsuji KOYAMA³

¹Faculty of Science, Nara Women's University, Kita-uoyanishimachi, Nara, Nara 630-8506, Japan

²Faculty of Education, Nara University of Education, Takabatake-cho, Nara, Nara 630-8528, Japan

³Department of Physics, Graduate School of Science, Kyoto University, Kitashirakawa-oiwake-cho, Sakyo-ku, Kyoto, Kyoto 606-8502, Japan

*yamauchi@cc.nara-wu.ac.jp

Received 2020 October 8; Accepted 2021 April 6

Abstract

The temperatures of the plasma in supernova remnants (SNRs) are initially very low just after the shock heating. The electron temperature (kT_e) increases quickly by Coulomb interaction, and then the energetic electrons gradually ionize atoms to increase the ionization temperature (kT_i). The observational fact is that most young and middle-to-old SNRs have lower kT_i than kT_e after the shock heating. The temperature evolution in shell-like SNRs has been explained by this ionizing plasma (IP) scenario. On the other hand, in the last decade, a significant fraction of mixed-morphology SNRs was found to exhibit a recombining plasma (RP) with higher kT_i than kT_e . The origin and the evolution mechanism of RP SNRs have been puzzling. To address this puzzle, this paper presents kT_e and kT_i profiles using follow-up Suzaku observations, and then proposes a new scenario for the temperature and morphology evolution in IP and RP SNRs.

Key words: ISM: supernova remnants — plasmas — radiation mechanisms: thermal — X-rays: ISM

1 Introduction

X-ray emitting thermal plasmas are found in shell-like supernova remnants (SNRs) and mixed-morphology (MM) SNRs (Rho & Petre 1998). The three important physical parameters that characterize the spectrum are the electron temperature (kT_e), ion (proton) temperature (kT_p), and ionization temperature (kT_i). The evolution of the thermal plasma of shell-like SNRs starts from shock heating by the blast wave (called the *adiabatic phase*) following free expansion (called the *free expansion phase*). At the start epoch of the adiabatic phase, kT_e and kT_i are very low. kT_p is also low, but is higher than kT_e because the larger mass of an ion (proton) provides higher energy than electrons. In the adiabatic phase, the protons transfer their energy

to the electrons, and increase kT_e in a short timescale. Then the electrons gradually ionize atoms to increase kT_i . Thus, most of the young shell-like SNRs have plasma with $kT_e > kT_i$, called ionizing plasma (IP; Masai 1994; Truelove & McKee 1999). After a long period of evolution, middle-to-old shell-like SNRs still have $kT_e > kT_i$ (IP), or become $kT_e \sim kT_i$ (collisional ionization equilibrium, CIE) at the end of the adiabatic phase, just before the *radiative cooling phase*.

This evolution scenario for IP in shell-like SNRs is well established in the theory (model) and observation (e.g. Tsunemi et al. 1986; Masai 1994; Truelove & McKee 1999). In the last decade, $kT_e < kT_i$ plasma (recombining plasma, RP) was found in a significant fraction of MM

SNRs (e.g. Hirayama et al. 2019, and references therein). One of the conventional scenarios is that cold clouds are responsible for both MM and RP SNRs; the evaporation of cold clouds makes extra thermal X-rays in the inner region of the SNR, transforming the shell structure to MM (White & Long 1991), and the same cold clouds decrease kT_e by thermal conduction, converting IP into RP.

Itoh and Masai (1989) proposed the rarefaction model, a unique model to explain the full evolution from IP to RP SNRs. Adiabatic expansion to low-density space causes rapid cooling of kT_e and makes RP. In the rarefaction model, the dense layer of circumstellar matter (CSM) causes reverse shock, producing a higher post-shock temperature than the case without dense CSM, and produces low-energy cosmic ray protons (LECRp) by the same process of diffusive shock acceleration in the blast wave (Shimizu et al. 2013). The rarefaction model, however, may not work for all RP SNR evolution; in actual SNRs, there may be many competing processes for the conversion of IP into RP. Cloud evaporation would be one example which is not considered in the rarefaction model. It may decrease kT_i , because of enhanced recombination by cool electrons in the dense CSM. Thus, although rarefaction is a unique model at present that can be successfully applied for the evolution to RP in some IP SNRs, it may not apply to all RP SNRs.

To evaluate which processes are actually operating in the evolution of RP SNRs, we propose a new scenario, which is free from theory and/or numerical calculation. We make kT_e and kT_i profiles which reflect the balance between the two competing processes, the increase of kT_i (enhanced ionization by LECRp) and the decrease of kT_i (enhanced recombination because of cool electrons from evaporated clouds). As for kT_e , there are complementary processes for electron cooling: adiabatic expansion, heat conduction from cold clouds, and energy loss by ionization. The observation-based temperature profiles lead us to a new scenario for the evolution of RP SNRs.

This paper is organized as follows. In section 2, high-quality spectra from five IP and four RP SNRs are taken from the archives of Suzaku (Mitsuda et al. 2007). Section 3 discusses the method and formalism of the spectral analysis for these SNRs, and then presents the fitting results of kT_i and kT_e for IP and RP SNRs. These results are compiled, and are used to construct the transition of RP from IP in section 4. Section 5 compares the conventional model and the new scenario, and discusses future prospects for an advanced picture of IP and RP evolution.

2 Selection of archive data

For comparison of IP and RP we utilized Suzaku archive data from the X-ray Imaging Spectrometer (XIS: Koyama et al. 2007) placed at the focal planes of the thin foil X-ray Telescopes (XRT: Serlemitsos et al. 2007). We selected the most reliable five IP and four RP SNRs, which are bright and/or have enough observational time, so that the best-fitting physical parameters have small errors, to precisely determine the SNR parameters. Among these, young IP SNRs are Cas A, Tycho, and SN 1006, and middle-to-old IP SNRs are CTB 109 and Cygnus Loop; a young RP SNR is W 49 B, and middle-to-old RP SNRs are IC 443, W 28, and G359.1–0.5. The observational logs of these SNRs are listed in table 1.

3 Analysis

3.1 Method of spectrum fit

To derive a unified picture for the evolution of RP and IP SNRs, we uniformly fitted the X-ray spectra of the nine selected SNRs (the *unified fit*). The X-ray spectra of the SNRs (source spectra) were obtained after subtracting the non-X-ray background (NXB, Tawa et al. 2008) and off-source sky background spectra (XB). The XB is either the Galactic off-plane spectra or the Galactic ridge spectra made by the method of Masui et al. (2009) for NXB or Uchiyama et al. (2013) for XB using the off-source sky region in the source fields listed in table 1.

The SNR spectra (source spectra) were fitted with a model having kT_i for each element, $kT_i(z)$, in the VVRNEI code of the XSPEC package (multi-VVRNEI model). The multi-VVRNEI model is z -dependent code, where the relevant elements were grouped to Mg–Ar (group A). The other elements were grouped in the order of atomic number (z): He–Ne is group B and Ca–Zn is group C.

The fitting model using the multi-VVRNEI code is

$$\sum_{z=H}^{z=Ni} \text{VVRNEI}[kT_e, kT_i(z), n_e t, \text{redshift}], \quad (1)$$

where n_e and t are the plasma density (cm^{-3}) and the evolution time (s), respectively. The other free parameter, *redshift*, is used for the fine-tuning of the possibly time-dependent energy scale (due to the calibration uncertainty) at the emission lines of the relevant elements.

In order to discuss the process of the evolution from IP to RP as essentially and clearly as possible, the spectral structure of Mg–Ar (group A) in the energy band of 1.3–4 keV was used because the essential difference between IP and RP was found near the K-shell lines of these elements.

Table 1. Observation logs of the selected SNRs.

Position	Observation ID	Start–end	Exposure time (ks)
IP SNRs			
		Cas A	
	100016010	2005-09-01 05:58:03–2005-09-01 18:20:14	28.0
		Tycho	
	500024010	2006-06-27 10:32:29–2006-06-29 15:40:24	101.1
		SN 1006	
SE	500016010	2006-01-30 09:01:20–2006-01-31 11:42:14	51.6
		CTB 109	
NE	506039010	2011-12-15 01:57:25–2011-12-15 18:03:11	30.4
SE	506040010	2011-12-15 18:03:52–2011-12-16 09:37:06	30.4
		Cygnus Loop	
NE1	500020010	2005-11-23 17:39:01–2005-11-24 04:55:24	20.4
NE2	500021010	2005-11-24 04:56:05–2005-11-24 16:14:24	21.4
NE3	500022010	2005-11-29 17:47:47–2005-11-30 05:39:09	21.7
NE4	500023010	2005-11-30 05:41:02–2005-11-30 18:23:14	25.3
RP SNRs			
		W 49 B	
	503084010	2009-03-29 02:33:12–2009-03-30 11:15:18	52.2
	503085010	2009-03-31 12:43:35–2009-04-02 01:28:20	61.4
		IC 443	
NE	501006010	2007-03-06 10:40:19–2007-03-07 12:22:14	42.0
NE	507015010	2012-09-27 05:29:48–2012-09-29 18:40:22	101.8
NE	507015020	2013-03-27 04:15:06–2013-03-28 16:00:19	59.3
NE	507015030	2013-03-31 11:44:34–2013-04-03 21:12:21	131.2
NE	507015040	2013-04-06 05:21:49–2013-04-08 02:00:21	75.6
		W 28	
Center	505005010	2010-04-03 07:23:22–2010-04-04 23:48:14	73.0
E	505006010	2011-02-25 10:54:11–2011-02-28 04:08:07	100.0
		G359.1–0.5	
W	502016010	2008-03-02 18:08:00–2008-03-04 17:40:19	70.5
S	502017010	2008-03-06 13:26:36–2008-03-08 16:00:24	72.5
N	503012010	2008-09-14 19:35:07–2008-09-16 00:50:14	57.7

In the fitting, the free parameters in group A were kT_e , $kT_i(z)$, $n_e t$, and the abundances. In group B, those of kT_e , kT_i , and $n_e t$ were linked to those of Mg. Group C was same as group B, but the free parameters were linked to those of Ar. We assumed all the abundances in groups B and C were ~ 1 solar.

Although the energy resolution in the early observations was not degraded by particle background, later observations were significantly degraded. The line broadening due to these time-dependent variations of the energy resolution and due to the spectrum sum are ~ 30 eV (FWHM). To compensate for these line broadenings, we applied the *gsmooth* code from the XSPEC package.

The spectra of many data sets (table 1) were merged into the final source spectra. The line broadening due to this merging effect can also be compensated by the *gsmooth* code. The spectrum of G359.1–0.5 with the unified fit is given in figure 1 as a typical example of the selected RP

SNRs. We see clear data excess at the energy of He α and Ly α , and radiative recombination continuum (RRC) of Si and S above the CIE model, as shown in figure 1b. Here, we call these excess the radiative recombination structure (RRS). The RRS was found in the residual of the CIE fit with $\chi^2/\text{d.o.f.}$ of 629/167 (figure 1b), and drastically disappears in the RP model fit with $\chi^2/\text{d.o.f.}$ of 206/165 (figure 1c). Therefore, the RRSs of Si and S can be used to judge whether the SNRs are RP or IP (or CIE). The sampled MM RP SNRs (W 49 B, IC 443, W 28, and G359.1–0.5) exhibited the clearest RRSs among the known MM RP SNRs.

3.2 The multi-VVRNEI fit

Using the multi-VVRNEI code, we carried out two model fittings, the $n_e t = 0$ fit and the free- $n_e t$ fit, for the IP SNRs. The $n_e t$ values in the free- $n_e t$ fit correspond to the

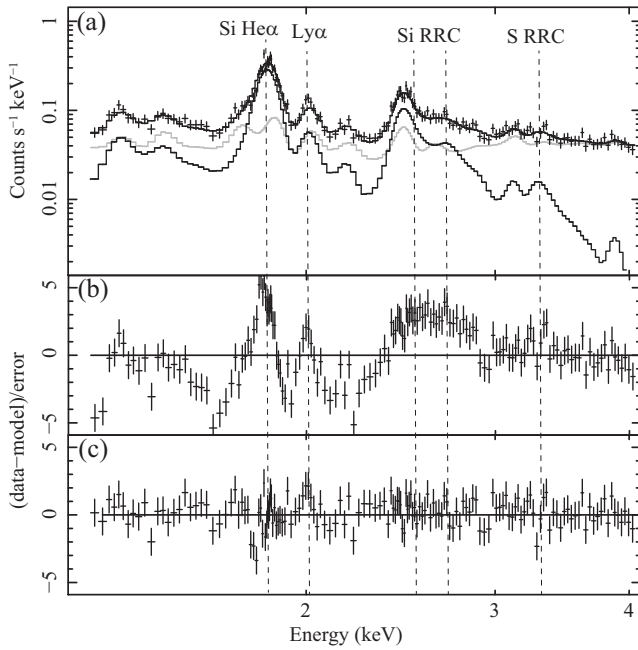


Fig. 1. (a) Spectrum of an RP SNR, G359.1–0.5 (sum of the XIS0 and 3 data, Koyama et al. 2007). The black and gray curves are the RP model for G359.1–0.5 and the background model, respectively. The dashed lines indicate the energies of Si, He α , and Ly α lines and the edge energies of Si and S RRCs. (b) Residuals of the spectrum for the CIE model (see text). (c) As panel (b), but for the RP model.

duration of the spectral evolutions from the starting epoch to the observed epoch. The best-fitting kT_e and $kT_i(z)$ for Mg, Si, S, and Ar in the $n_e t = 0$ fit (observed epoch) and $n_e t$ in the free- $n_e t$ fit for each IP SNR are listed in table 2. We also fitted the RP SNR spectra with fixed $n_e t = 0$ and free- $n_e t$. The $n_e t$ values obtained from the free- $n_e t$ fit for the RP SNRs do not correspond to the SNR ages, but correspond to the elapsed time after the transition to the RP phase. The best-fitting parameters are listed in table 3.

Table 2. Best-fitting parameters for IP SNRs.*

	Cas A	Tycho	SN 1006	CTB 109	Cygnus Loop
Observed epoch ($n_e t = 0 \text{ cm}^{-3} \text{ s}$)					
kT_e	3.09 ± 0.04	1.76 ± 0.02	0.98 ± 0.04	0.57 ± 0.03	0.30 ± 0.01
$kT_i(\text{Mg})^\dagger$	0.59 ± 0.01	0.50 ± 0.02	0.09 ± 0.01	0.49 ± 0.02	0.30 ± 0.05
$kT_i(\text{Si})^\dagger$	0.78 ± 0.01	0.56 ± 0.01	0.13 ± 0.01	0.57 ± 0.05	0.29 ± 0.05
$kT_i(\text{S})^\dagger$	0.99 ± 0.01	0.68 ± 0.02	0.18 ± 0.01	‡	‡
$kT_i(\text{Ar})^\dagger$	1.47 ± 0.01	0.84 ± 0.01	0.25 ± 0.03	‡	‡
$\chi^2/\text{d.o.f.}$	1721/744 (2.31)	2577/720 (3.58)	447/373 (1.20)	343/265 (1.29)	269/269 (1.00)
$n_e t$ free					
$n_e t \text{ (cm}^{-3} \text{ s)}$	$(5.2 \pm 0.1) \times 10^{10}$	$(2.9 \pm 0.1) \times 10^{10}$	$(6.3 \pm 0.7) \times 10^9$	$(6.3 \pm 0.8) \times 10^{11}$	$(3.0 \pm 1.7) \times 10^{12}$

*Assuming the plasma density, $n_e \text{ (cm}^{-3}\text{)}$, is 1 cm^{-3} , $t \text{ (s)}$ from the best-fitting $n_e t$ value in the $n_e t$ free fitting is the age of the IP SNR.

†Units are keV.

‡Not determined due to poor data in the high- z elements.

4 Results and unified picture of IP and RP SNRs

4.1 The kT_i distribution with z in IP and RP SNRs

The kT_i distribution of each SNR as a function of z is plotted in figure 2. The following facts can be observed:

- The kT_i values in both the IP and RP SNRs are smaller for smaller z , and have similar shapes to each other.
- The kT_i values of RP SNRs are larger than those of IP SNRs.

Sawada and Koyama (2012) compared the element-dependent $kT_i(z)$ profile for CIE and the IP process in the spectrum of RP SNR W 28. The element-dependent $kT_i(z)$ profile for RP SNR W 28 is consistent with our result (i). Facts (i) and (ii) naturally lead to the idea that an RP SNR comes after the well-established phase in the shell-like IP SNR. In this idea, the RP SNR phase smoothly follows on from an IP process (IP SNR).

4.2 The kT_e distribution in IP SNRs

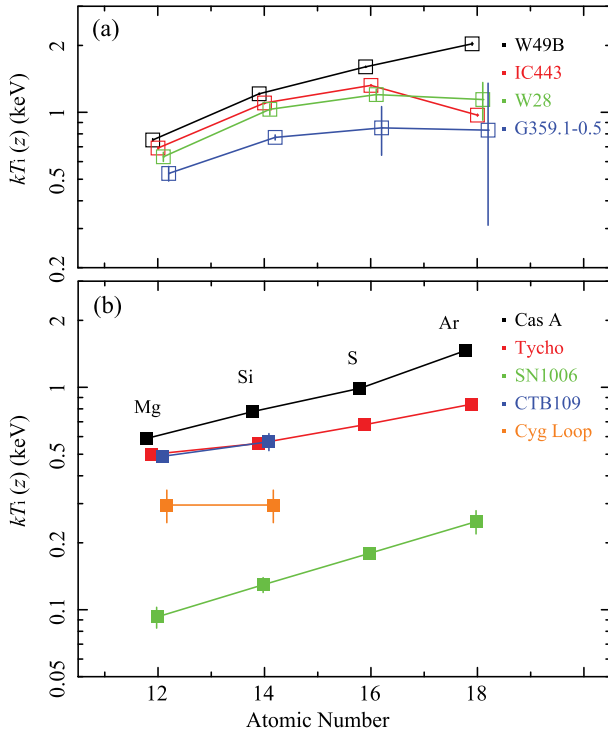
The X-ray spectra of SNR plasma is mainly composed of line and continuum emissions. The former, mainly He α and Ly α , is determined by kT_i , while the latter is determined by kT_e . Thus, kT_e represents the main component in the hot plasma, almost independent of kT_i (insensitive to IP or RP). The evolution curve of the similarity solution (Sedov 1959) predicts that kT_e is a power-law function with an index of $6/5$ as a function of age (t). However, the real kT_e evolution curve may be significantly modified by thermal conduction from cold cloud, energy transfer from protons ($kT_p > kT_e$ in young SNRs; Rakowski et al. 2003), energy-dependent competing processes (ionization and recombination), or others. Details of these processes are complicated, and hence not very predictable. Furthermore, these processes are coupled with each other, and hence theoretical

Table 3. Best-fitting parameters for RP SNRs.*

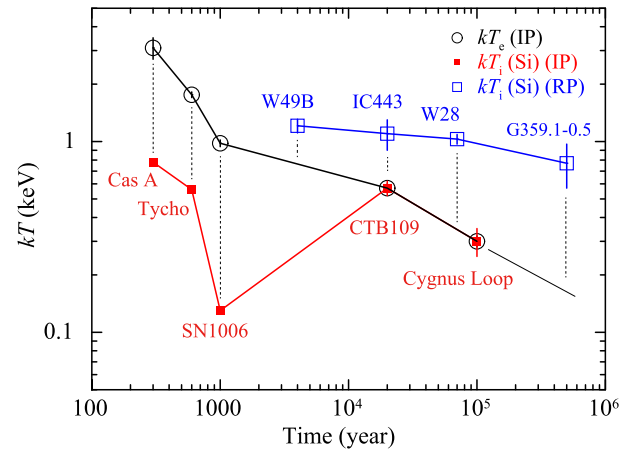
	W 49 B	IC 443	W 28	G359.1–0.5
Observed epoch ($n_e t = 0 \text{ cm}^{-3} \text{ s}$)				
kT_e^\dagger	0.75 ± 0.01	0.55 ± 0.01	0.33 ± 0.05	0.16 ± 0.02
$kT_i(\text{Mg})^\dagger$	0.75 ± 0.01	0.69 ± 0.01	0.63 ± 0.03	0.53 ± 0.04
$kT_i(\text{Si})^\dagger$	1.21 ± 0.01	1.10 ± 0.01	1.03 ± 0.06	0.77 ± 0.02
$kT_i(\text{S})^\dagger$	1.60 ± 0.01	1.33 ± 0.01	1.20 ± 0.07	0.85 ± 0.21
$kT_i(\text{Ar})^\dagger$	2.03 ± 0.03	1.00 ± 0.01	1.14 ± 0.22	0.83 ± 0.52
$\chi^2/\text{d.o.f.}$	558/344 (1.62)	1148/583 (1.97)	365/335 (1.09)	381/363 (1.05)
$n_e t$ free				
$n_e t \text{ (cm}^{-3} \text{ s)}$	$(2.8 \pm 0.2) \times 10^{11}$	$(2.7 \pm 0.1) \times 10^{11}$	$< 1.0 \times 10^{11}$	$1.5^{+5.0}_{-1.4} \times 10^{11}$

*Assuming the plasma density, $n_e \text{ (cm}^{-3}\text{)}$, is 1 cm^{-3} , $t \text{ (s)}$ from the best-fitting $n_e t$ value in the $n_e t$ free fitting is the duration time of the RP phase of the RP SNR.

†Units are keV.

**Fig. 2.** $kT_i(z)$ distribution of selected (a) RP and (b) IP SNRs as a function of z . (Color online)

prediction of the kT_e evolution curve is not available at present. We therefore make the kT_e evolution curve of IP SNRs at the best-fitting position of the $n_e t = 0$ fit (black solid line in figure 3). For young IP SNRs (Cas A, Tycho, and SN 1006), well-established ages were used, while those for older SNRs (CTB 109 and Cygnus Loop) were estimated using the best-fitting value of $t = n_e t / n_e$. Since the evolution of kT_e in IP SNRs starts from the initial epoch of the adiabatic phase, t is regarded approximately to be the SNR age, if n_e has the typical value of 1 cm^{-3} . This evolution curve shows a monotonic decrease with the age t , qualitatively similar to the Sedov solution. As we noted before, the kT_e evolution curve of RP SNRs should be similar to that of the

**Fig. 3.** Empirical evolution curve for the selected samples of IP and RP SNRs. The open and filled symbols are kT_e and kT_i (Si). The evolution curve of kT_e for IP in the adiabatic expansion phase and that of kT_i are shown by the black and red lines, respectively. The evolution curve of kT_i for RP is shown by the blue line. The dashed lines are to guide the eye for the evolution of kT_e for IP and RP as a function of $n_e t$. The values on the horizontal axis are the SNR ages (the epoch is the start of the adiabatic phase), where the ages $> 10^4$ yr (CTB 109 and Cygnus Loop) are estimated from the best-fitting $n_e t$ for $n_e = 1 \text{ cm}^{-3}$. (Color online)

IP SNRs. The youngest RP, W 49 B, has $kT_e \sim 0.8 \text{ keV}$ in the $n_e t = 0$ fit at the epoch of the observing time (table 3).

For kT_e for W 49 B, Ozawa et al. (2009) and Yamaguchi et al. (2018) reported $\sim 1.1\text{--}1.8 \text{ keV}$, nearly 1.3–2.3 times $\sim 0.8 \text{ keV}$. However, these values were determined in the hard energy bands of 5–12 keV (Ozawa et al. 2009) or 3–20 keV (Yamaguchi et al. 2018). On the other hand, this paper has used the softer band of 1.3–4 keV. Furthermore, the kT_e values of Ozawa et al. (2009) and Yamaguchi et al. (2018) are those at the start epoch of the RP phase ($n_e t$ -free fit), while this paper is at the observed epoch ($n_e t = 0$ fit). Thus, the larger kT_e of Ozawa et al. (2009) and Yamaguchi et al. (2018) rather than the one from this paper may be reasonable. The kT_e value of W 49 B corresponds to the kT_e of an IP SNR between SN 1006 and CTB 109. Therefore,

the best-fitting kT_e of W49 B (RP) is placed on the kT_e evolution curve of IP SNRs at a position near SN 1006 and CTB 109. Likewise, we placed the kT_e values of the middle-to-old RP SNRs (IC 443, W28, and G359.1–0.5) near the positions of the middle-to-old IP SNRs (CTB 109 and Cygnus Loop).

In the young IP SNRs kT_i is smaller than kT_e , while in the old SNRs (CTB 109 and Cygnus Loop) kT_i becomes almost equal to kT_e (figure 3). kT_e peaks for Cas A (age ~ 300 yr), and monotonically decreases with increasing age. This indicates that the adiabatic phase starts near 300 yr after the free expansion phase (Sedov 1959). In the evolution of middle-to-old IP SNRs, the epoch when the kT_i (Si) value becomes equal to that of kT_e is at the age of CTB 109. This indicates that the ionization timescale is $\sim 2 \times 10^4$ yr, which is significantly smaller than the recombination timescale. The evolution continues keeping the balance of recombination rate \simeq ionization rate.

4.3 Difference in kT_i (Si) profile between IP and RP SNRs

The kT_i (Si) profiles of the IP SNRs are given in figure 3 by filled squares, while the red solid line connects the data points (the kT_i (Si) profile). The open squares in figure 3 are the kT_i (Si) profile of the RP SNRs, while the blue line connects them. The kT_i (Si) profile must be different between IP and RP SNRs, because the line fluxes and the RRS of the key element Si are due to a local two-body process in ionization and/or recombination. As we mentioned in subsection 4.2, Cas A, Tycho, and SN 1006 are historical SNRs, and hence their ages are either well predicted (Cas A) or we have the actually observed date of the SNRs (Tycho and SN 1006). For the other two, we estimated the ages using the best-fitting $n_e t$ values. On the other hand, we cannot find any reports for the age or elapsed time in the RP phase. Thus, interpolating the kT_e values between IP and RP SNRs, we determined the horizontal positions for RP SNRs.

The young RP SNR W49 B would have changed to the RP phase due to the extra ionization. At the epoch of this phase change, kT_i (Si), ~ 1.2 keV, is higher than kT_e , ~ 0.8 keV. No kT_i data for RP SNRs that are younger than $\sim 10^3$ yr are found among our selected samples.¹ For the middle-to-old SNRs (IC 443, W28, and G359.1–0.5), the kT_i (Si) profile is systematically higher than those of the middle-to-old IP SNRs (CTB 109 and Cygnus Loop).

5 Discussion and future prospects

Using the observed data and the results of the multi-VVRNEI model fit, we made three evolution curves: kT_e (I), and kT_i (Si) of RP (II) and IP (III) SNRs. The new idea of this scheme is that we can determine kT_i and kT_e at the observed epoch with the VVRNEI code of the $n_e t = 0$ fit. We note that conventional VVRNEI analysis predicts no kT_i value at the observation epoch.

In the kT_e profile (I), a critical assumption is that the kT_e curves of IP and RP are similar. This assumption is based on the fact that kT_e is determined by the global, dynamical evolution of the thermal plasma. One problem is that the age estimation (using the $n_e t$ value in the free $n_e t$ fit) of the middle-to-old SNRs has significant ambiguities and/or statistical errors. For example, the best-fitting $n_e t$ values of CTB 109 and Cygnus Loop give their ages as $(2.0 \pm 0.3) \times 10^4$ and $(9.5 \pm 5.4) \times 10^4$ yr, respectively. Within these errors, the important conclusion that kT_e has a monotonic decrease with slow rate as a function of SNR age t (figure 3) is not changed.

In the kT_i (Si) profile of the RP SNRs (II), the kT_i value of the young SNR ($< 10^4$ yr) W49 B is plotted as ~ 1 keV at the position of the IP SNR line of $kT_e \sim 0.8$ keV, while that in the old SNR ($> 10^5$ yr) G359.1–0.1 is plotted as ~ 0.7 keV at the IP SNR line of $kT_e \sim 0.2$ keV. Then, kT_i (Si) for the RP SNRs shows a very slow decrease with increasing $n_e t$.

For the IP SNRs (III), unlike the RP SNRs, kT_i (Si) has a local minimum at the epoch of $t \sim 10^3$ yr (at the position of SN 1006). The lower ionization temperature in SN 1006 than the expectation from the overall trend would be due to the difference in the density. SN 1006 is known to have a low-density environment (e.g. Dubner et al. 2002) and therefore the thermal evolution of its shock-heated ejecta is slower than the others (e.g. Yamaguchi et al. 2008).

In the old age of the low kT_e region, the recombination rate becomes nearly equal to the ionization rate, hence kT_i (Si) saturates near the kT_e values (after the position of CTB 109). The observational fact that kT_i values of RP SNRs are much higher than those of any IP SNRs implies that the RP originates from some extra ionization rather than cooling of kT_e as suggested in the conduction and rarefaction models. Based on these three observational profiles, we propose a new scheme for a unified picture for IP and RP evolution. In this scheme, an essential player is small cloudlets. The small cloudlets would produce LECRp by diffusive shock acceleration in the hot plasma. LECRp is the most likely source of additional ionization, and then the plasma changes from IP to RP (phase transition in the ionization state), when the kT_e value of RP gradually becomes equal to that of IP in the full evolution history. The cloudlets also make diffuse hot plasma in the interior

¹ The age estimation in this paper is based on the best-fitting $n_e t$. As we noted, this age estimation is not reliable for RP SNRs, and hence should be regarded conservatively.

of SNRs surrounded by a shell. This causes another phase transition from shell-like to MM SNRs (phase transition in morphology).

The profiles (I), (II), and (III) were made from limited samples of SNR data with high-quality spectra. This is a weak point in our scenario (biased picture). To make an unbiased picture, we encourage observations of greater numbers of IP and RP SNRs with high energy resolution and statistics. The next Japanese-led mission, X-Ray Imaging and Spectroscopy Mission (XRISM), has a high capability of X-ray spectroscopy using a microcalorimeter, which would be suitable for such observations. This can be powerful for the study of line flux and width in the energy band of the RRS, which would distinguish SNRs between IP and RP. It also provides key information for the study of the origin of RP and the transition mechanism from IP to RP. Then, the reliability of our unified scenario for the temperature and morphology evolution in both IP and RP SNRs should become higher than our present scenario.

References

- Dubner, G. M., Giacani, E. B., Goss, W. M., Green, A. J., & Nyman, L.-Å. 2002, *A&A*, 387, 1047
- Hirayama, A., Yamauchi, S., Nobukawa, K. K., Nobukawa, M., & Koyama, K. 2019, *PASJ*, 71, 37
- Itoh, H., & Masai, K. 1989, *MNRAS*, 236, 885
- Koyama, K., et al. 2007, *PASJ*, 59, S23
- Masai, K. 1994, *ApJ*, 437, 770
- Masui, K., Mitsuda, K., Yamasaki, N. Y., Takei, Y., Kimura, S., Yoshino, T., & McCammon, D. 2009, *PASJ*, 61, S115
- Mitsuda, K., et al. 2007, *PASJ*, 59, S1
- Ozawa, M., Koyama, K., Yamaguchi, H., Masai, K., & Tamagawa, T. 2009, *ApJ*, 706, L71
- Rakowski, C. E., Ghavamian, P., & Hughes, J. P. 2003, *ApJ*, 590, 846
- Rho, J., & Petre, R. 1998, *ApJ*, 503, L167
- Sawada, M., & Koyama, K. 2012, *PASJ*, 64, 81
- Sedov, L. I. 1959, *Similarity and Dimensional Methods in Mechanics* (New York: Academic Press)
- Serlemitsos, P. J., et al. 2007, *PASJ*, 59, S9
- Shimizu, T., Masai, K., & Koyama, K. 2013, *PASJ*, 65, 69
- Tawa, N., et al. 2008, *PASJ*, 60, S11
- Truelove, J. K., & McKee, C. F. 1999, *ApJS*, 120, 299
- Tsunemi, H., Yamashita, K., Masai, K., Hayakawa, S., & Koyama, K. 1986, *ApJ*, 306, 248
- Uchiyama, H., Nobukawa, M., Tsuru, T. G., & Koyama, K. 2013, *PASJ*, 65, 19
- White, R. L., & Long, K. S. 1991, *ApJ*, 373, 543
- Yamaguchi, H., et al. 2008, *PASJ*, 60, S141
- Yamaguchi, H., et al. 2018, *ApJ*, 868, L35